

Nature of long-lived moiré interlayer excitons in electrically tunable $\text{MoS}_2/\text{MoSe}_2$ heterobilayers

Evgeny M. Alexeev,^{*,†,‡} Carola M. Purser,^{‡,†} Carmem M. Gilardoni,[‡] James Kerfoot,[†] Hao Chen,[†] Alisson R. Cadore,^{†,¶} Bárbara L.T. Rosa,[†] Matthew S. G. Feuer,[‡] Evans Javary,^{‡,§} Patrick Hays,^{||} Kenji Watanabe,[⊥] Takashi Taniguchi,[#] Seth Ariel Tongay,^{||} Dhiren M. Kara,[‡] Mete Atatüre,^{*,‡} and Andrea C. Ferrari^{*,†}

[†]*Cambridge Graphene Centre, University of Cambridge, 9 JJ Thomson Avenue, CB3 0FA, Cambridge, UK*

[‡]*Cavendish Laboratory, University of Cambridge, JJ Thomson Avenue, Cambridge CB3 0HE, UK*

[¶]*Brazilian Nanotechnology National Laboratory, Brazilian Center for Research in Energy and Materials, Sao Paulo, Brazil*

[§]*École Normale Supérieure, PSL, 5 Rue D'ulm Paris, 75005, France*

^{||}*Materials Science and Engineering, School for Engineering of Matter, Transport and Energy, Arizona State University, Tempe, Arizona 85287, United States*

[⊥]*Research Center for Electronic and Optical Materials, National Institute for Materials Science, 1-1 Namiki, Tsukuba 305-0044, Japan*

[#]*Research Center for Materials Nanoarchitectonics, National Institute for Materials Science, 1-1 Namiki, Tsukuba 305-0044, Japan*

E-mail: ea529@cam.ac.uk; ma424@cam.ac.uk; acf26@cam.ac.uk

Abstract

Interlayer excitons in transition-metal dichalcogenide heterobilayers combine high binding energy and valley-contrasting physics with long optical lifetime and strong dipolar character. Their permanent electric dipole enables electric-field control of emission energy, lifetime, and location. Device material and geometry impacts the nature of the interlayer excitons via their real- and momentum-space configurations. Here, we show that interlayer excitons in MoS₂/MoSe₂ heterobilayers are formed by charge carriers residing at the Brillouin zone edges, with negligible interlayer hybridization. We find that the moiré superlattice leads to the reversal of the valley-dependent optical selection rules, yielding a positively valued g-factor and cross-polarized photoluminescence. Time-resolved photoluminescence measurements reveal that the interlayer exciton population retains the optically induced valley polarization throughout its microsecond-long lifetime. The combination of long optical lifetime and valley polarization retention makes MoS₂/MoSe₂ heterobilayers a promising platform for studying fundamental bosonic interactions and developing excitonic circuits for optical information processing.

Keywords

van der Waals heterostructures, transition metal dichalcogenides, interlayer excitons, moiré superlattice, valley polarization, Stark shift, photoluminescence

Van der Waals heterostructures comprising monolayer transition-metal dichalcogenides (TMDs) have emerged as a promising platform for optoelectronics¹⁻⁴ and quantum technology⁵ as they combine optically addressable spin and valley degrees of freedom⁶⁻⁸ with unique tunability through the choice of material combination⁹⁻¹¹ and rotational alignment.¹²⁻¹⁴ TMD heterobilayers have drawn particular interest due to their ability to host interlayer excitons (iXs)^{15,16} which offer lifetime approaching 200 μs ,¹⁷ strong repulsive dipolar interaction,^{18,19} and high sensitivity to rotational alignment,²⁰⁻²² strain,^{17,23} electric²⁴ and magnetic²⁵ fields. Different TMD combinations give rise to iX with drastically different properties, including oscillator strength,^{26,27} center-of-mass momentum,^{20,21} and degree of interlayer hybridization.^{19,22} Of the plethora of possible TMD combinations, the majority of research effort focused on $\text{MoSe}_2/\text{WSe}_2$ ²⁷⁻³⁰ and WS_2/WSe_2 ³¹⁻³³ heterobilayers. For other material combinations, key aspects of iX nature, such as real- and momentum-space configuration, remain elusive due to the complexity of the underlying physics.

In this work, we investigate iX in $\text{MoS}_2/\text{MoSe}_2$ heterobilayers using polarization-resolved magneto-photoluminescence spectroscopy. We find that iX photoluminescence (PL) is visible only in devices with relative twist angle less than 5° . This indicates that the constituent iX charge carriers reside at the edges of the Brillouin zone. We study the iX PL response to out-of-plane electric and magnetic fields and show that iX is formed by charge carriers at the $\pm\text{K}$ valleys with negligible degree of interlayer hybridization. Our time- and polarization-resolved PL measurements reveal microsecond-scale retention of optically induced valley polarization, demonstrating the potential of $\text{MoS}_2/\text{MoSe}_2$ heterobilayers for opto-valleytronic applications.

Figure 1a shows an optical microscope image of one of our electric-field tunable $\text{MoS}_2/\text{MoSe}_2$ heterobilayers, with panel b displaying its cross-section. The hexagonal boron nitride layers provide a flat and clean dielectric environment for the $\text{MoS}_2/\text{MoSe}_2$ heterobilayer, and the transparent few-layer graphene top and bottom gates allow optical measurements under applied out-of-plane electric field. Each of the eight devices is fabricated from micromechanically exfoliated crystals using deterministic dry mechanical transfer,^{34,35} and thickness and

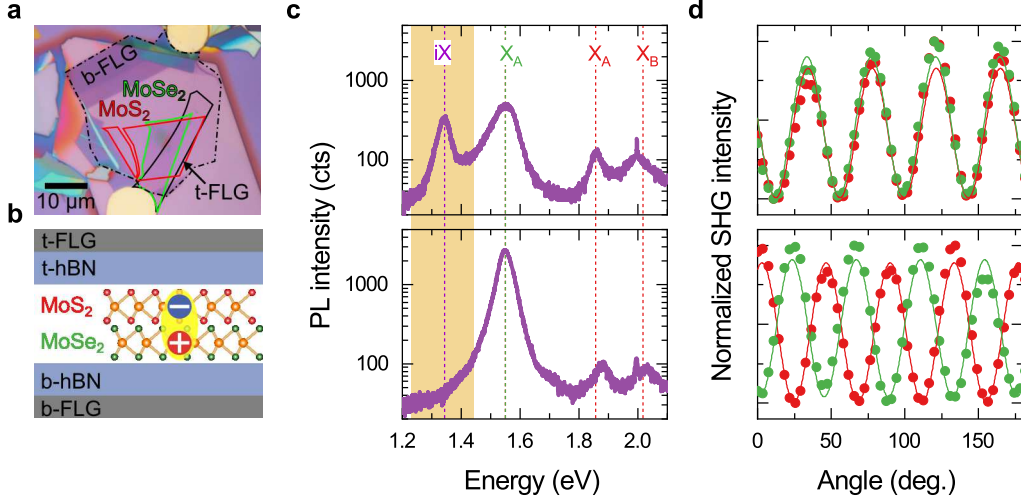


Figure 1: **iX in MoS₂/MoSe₂ heterobilayers.** (a) Optical microscope image of an electrically tunable MoS₂/MoSe₂ heterobilayer device. Monolayer MoS₂ and MoSe₂ regions are outlined in red and green, respectively. Solid (dashed) black line shows the position of top (bottom) gate composed of few-layer graphene (FLG) (b) Cross-sectional schematic of the device structure, indicating spatial configuration of iX. (c) Room-temperature PL spectra recorded in two devices with different rotational alignment. The closely rotationally aligned device (top panel, $\theta = 1^\circ$) shows intralayer MoS₂ B and A excitons and MoSe₂ A exciton peaks, as well as an iX peak appearing in a lower-energy range (highlighted in copper) that is not visible in the PL spectrum of the strongly misaligned device (bottom panel, $\theta = 28^\circ$). (d) Polarization-resolved SHG intensity recorded in the isolated monolayer (red) MoS₂ and (green) MoSe₂ regions of the two devices, confirming the twist angle of $\theta = 1^\circ$ (top) and $\theta = 28^\circ$ (bottom).

quality of constituent layers are characterized using Raman spectroscopy³⁶ (see Methods and SI Fig. S1). The devices offer a range of twist angles between the TMD monolayers θ , enabling the investigation of iX momentum-space configuration. Figure 1c compares room-temperature PL spectra of two devices with twist angle $\theta = 1^\circ$ (top) and $\theta = 28^\circ$ (bottom). We identify θ using polarization-resolved second-harmonic generation (SHG) measurements (Fig. 1d). Both devices show PL peaks corresponding to the A exciton in MoSe₂ (MoSe₂ X_A) at 1.55 eV and the A and B excitons in MoS₂ (MoS₂ X_A and X_B) at 1.85 and 2.0 eV, respectively.^{37,38} Crucially, the iX PL peak at ~ 1.3 eV is visible only in the device with $\theta = 1^\circ$. Of the eight devices with twist angles ranging from 1° to 28° that we studied, only those with $\theta \leq 5^\circ$ reveal the iX PL peak at room temperature (SI Fig. S2), in line with a recent report.³⁹ Thus, close rotational alignment is critical for the observation of iX in

MoS₂/MoSe₂ heterobilayers.

The $\sim 3.7\%$ mismatch in lattice constants of MoS₂ and MoSe₂⁴⁰ eliminates twist-angle dependence of the interlayer distance as an underlying source of this behavior.⁴¹ Instead, the high sensitivity of the iX PL intensity to θ indicates that the iX is formed by the charge carriers residing in valleys at the edges of the Brillouin zone. Homo- and heterobilayers where at least one of the charge carriers resides at the Γ valley at the center of the Brillouin zone display iX PL throughout the entire θ range, as the momentum-space separation between electron and hole remains unchanged.^{21,42,43} In contrast, in heterobilayers where both constituent charges reside at the edges of the Brillouin zone, momentum-space separation of electron and hole suppresses radiative recombination of iX in devices with θ away from 0 or 60°,^{13,20} consistent with our observations.

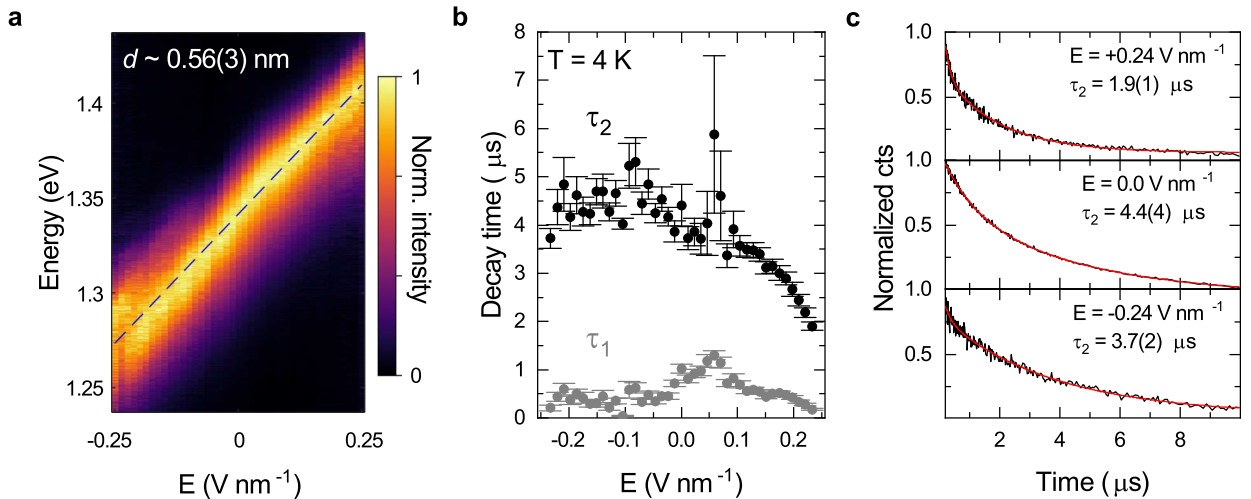


Figure 2: **Electric field tuning of iX.** (a) Normalized iX PL under applied out-of-plane electric field. iX PL energy shows a linear shift with the slope of ~ 0.31 eV nm V⁻¹, corresponding to the dipole size of $d = 0.56(3)$ nm. The dipole size closely matches the expected interlayer distance. (b) Variation of iX PL decay time as a function of applied electric field. Gray and black circles correspond to the fast (τ_1) and slow (τ_2) time constants, respectively. (c) PL decay acquired at $+0.24$, 0 , and -0.24 V nm⁻¹ applied electric field. Red curves are bi-exponential fits to the data.

We next identify the real-space configuration of iX by studying its response to applied out-of-plane electric field. Figure 2a presents the normalized iX PL spectrum recorded as

a function of electric field at 4-K temperature. The iX PL energy shifts linearly with a rate of ~ 0.31 eV nm V^{-1} and can be tuned over a 144-meV range within the gate tuning limits of our device. We find an average tuning response across three devices of ~ 0.30 eV nm V^{-1} , yielding an average dipole size of $0.55(3)$ nm^{19,24} (SI Fig. S3). This value is in good agreement with the ~ 0.6 -nm separation between the layers.⁴⁴ A similar dipole size was observed in MoSe₂/WSe₂¹⁹ heterobilayers with iX is formed by non-hybridized electrons and holes, while MoSe₂ homobilayers show a reduced dipole size of 0.26 nm due to charge-carrier hybridization.⁴⁵ Comparatively, our results suggest negligible interlayer hybridization for our devices.

Figure 2b shows the iX PL decay time constants as a function of the applied electric field. We extract these constants from a bi-exponential fit to the time-resolved PL. Figure 2c presents examples of PL decay trace recorded at three applied field values along with their corresponding fit curves. We observe microsecond-long iX lifetime, with a fast time constant $\tau_1 = 1.0(1)$ μ s and a slow time constant $\tau_2 = 4.4(4)$ μ s at zero electric field – an order of magnitude longer than typical lifetimes of 10-100 ns reported for MoSe₂/WSe₂ heterobilayers.¹³ The slow time constant in other devices ranges from 0.1 μ s to 3.0 μ s (SI Fig. S4). The fast time constant is mostly field-independent, except for ~ 0.06 V nm⁻¹, where it increases to 1.3 μ s. Shortening of τ_1 for electric field away from this value is likely caused by inadvertent electrostatic doping induced by a slight asymmetry in the thicknesses of the bottom and top dielectric layers. The slow time constant τ_2 shows a gradual decrease with increasing electric field, consistent with a change in radiative lifetime due to a field-induced variation of electron-hole separation. For electric field anti-parallel to the electric dipole moment of the iX, the separation between the two charge carriers is reduced, leading to an increased probability of their radiative recombination. The opposite process takes place for the parallel field alignment. That said, the PL decay time remains slow ($\tau_1 \geq 0.04$ μ s, $\tau_2 \geq 1.9$ μ s) throughout the entire field-tuning range.

We use polarization-resolved magneto-PL spectroscopy to identify valley configuration of

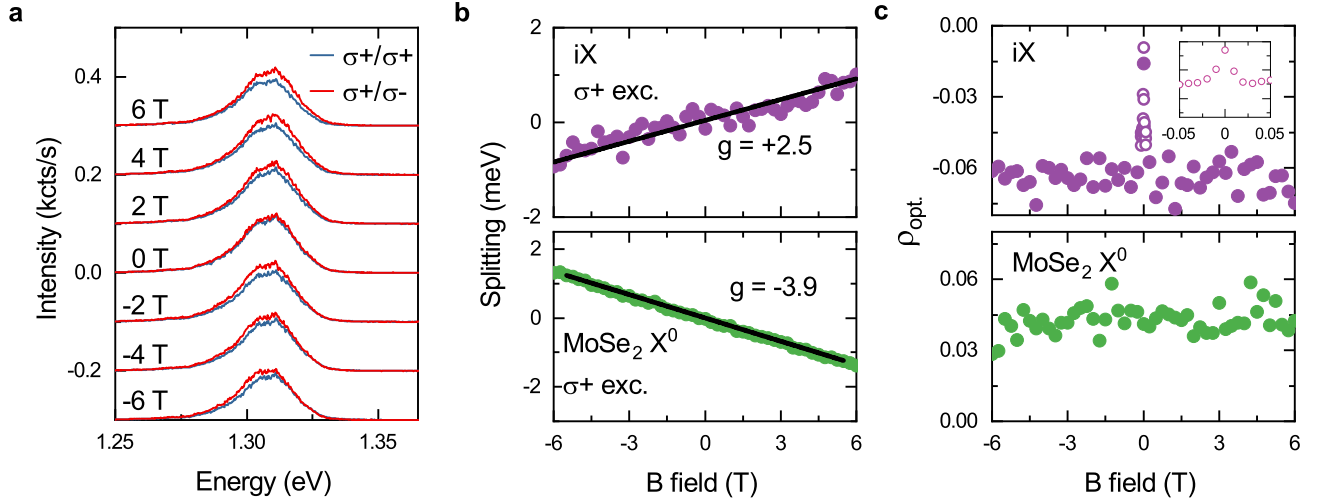


Figure 3: **Magneto-PL spectroscopy of iX.** (a) Helicity-resolved iX PL spectra recorded under applied out-of-plane magnetic field ranging from -6 to 6 T using σ^+ polarized 1.94 eV optical excitation; blue (red) curves correspond to PL with σ^+ (σ^-) polarization. (b) Energy splitting between σ^+ and σ^- polarized PL as a function of out-of-plane magnetic field for (top) iX in heterobilayer and (bottom) neutral excitons (X^0) in MoSe₂ monolayer regions. Landé g-factors extracted using linear fits are listed next to each plot. (c) Optically induced valley polarization calculated as $\rho_{\text{opt}} = (I^{++} + I^{--} - I^{+-} - I^{-+}) / (I^{++} + I^{--} + I^{+-} + I^{-+})$ as a function of magnetic field for iX (top) and MoSe₂ X^0 (bottom), where I^{XY} is the intensity of PL with σ^Y -polarization collected under σ^X -polarized excitation. Unfilled circles in the panel and the inset are extracted from a fine scan around 0 T, showing the small-field dependence of ρ_{opt} for iX.

iX. Figure 3a shows iX PL spectra recorded using right circularly polarized (σ^+), 1.94-eV excitation as a function of applied out-of-plane magnetic field B ranging from -6 to 6 T; blue (red) curves correspond to PL with σ^+ (σ^-) polarization. The iX PL remains cross-polarized with respect to the excitation laser throughout the entire magnetic field range. Two distinct mechanisms are known to give rise to this behavior in TMD heterobilayers: the directional intervalley scattering⁴⁶ and the moiré-induced reversal of the valley-dependent optical selection rules.⁴⁷

We identify the underlying mechanism in MoS₂/MoSe₂ heterobilayers based on the sign of the energy splitting between σ^+ and σ^- polarized PL under applied magnetic field. Figure 3b is a plot of the energy splitting (ΔE) as a function of B for the iX in the heterobilayer region (top panel) and the neutral intralayer excitons (X^0) in an isolated monolayer MoSe₂ region

(bottom panel). We define ΔE as $E_{\sigma^+} - E_{\sigma^-} = g\mu_B B$, where E_{σ^+} (E_{σ^-}) is the energy of the σ^+ (σ^-) polarized PL, g is the effective Landé g-factor and μ_B is the Bohr magneton. For X^0 in MoSe₂, we extract $g = -3.90(2)$, consistent with previous reports,⁴⁸ where the minus sign stems from valley-Zeeman interaction and valley-dependent optical selection rules for TMD monolayers:⁴⁹ σ^+ -polarized light couples to optical transitions in the +K valley, which has lower energy at positive B . In contrast, we obtain $g = +2.50(7)$ for iX - the positive sign of g shows that iX PL from the +K valley appears with σ^- polarization, confirming the reversal of optical selection rules with respect to the monolayer case. All devices showed positive iX g-factors, with an average value of +4.5. In TMD heterobilayers, the reversal of the selection rules arises from local changes in crystal symmetry induced by the moiré superlattice.⁴⁷ We observe the iX g-factors ranging from +1.0 to +8.0, likely due to the difference in the moiré pattern parameters arising from different twist angles and local strain in different devices (see SI Fig. S5).

Two mechanisms can give rise to the observed PL polarization under finite magnetic field, namely the optically induced valley polarization⁵⁰ and the Zeeman-shift-induced valley thermalization.³⁷ The former is limited by non-directional intervalley scattering, while the latter arises from exciton relaxation into the lower-energy valley. We calculate the degree of optically induced valley polarization independently as $\rho_{\text{opt}} = \frac{I^{++}+I^{--}-I^{+-}-I^{-+}}{I^{++}+I^{--}+I^{+-}+I^{-+}}$, where I^{XY} represents the intensity of PL with σ^Y -polarization collected under σ^X -polarized excitation. Figure 3c displays the dependence of ρ_{opt} on the applied magnetic field for iX and MoSe₂ X^0 . MoSe₂ X^0 shows a constant PL polarization degree of $\sim 4\%$, consistent with earlier reports.^{51,52} In contrast, $|\rho_{\text{opt}}|$ for iX shows a distinct increase with increasing $|B|$, saturating at $\sim 6\%$ above ± 20 mT (see inset in Fig. 3c). This dependence is consistent across all devices, with $|\rho_{\text{opt}}|$ ranging from 6% to 14% maximum value. In the absence of magnetic field, $|\rho_{\text{opt}}|$ ranges from 0% to 7%. Similar sharp changes in valley polarization degree with applied magnetic field have been observed for iX in MoSe₂/WSe₂⁵³ and MoS₂/WSe₂⁵⁴ heterobilayers, as well as intralayer excitons in WS₂ and WSe₂ monolayers.⁵⁵ This effect was attributed to

the suppression of intervalley scattering of intralayer excitons within the monolayer with dark excitonic ground state.⁶ However, we observe device-specific saturation field for $\rho_{\text{opt}} (B_{\text{sat}})$ ranging from 0.02 to 3 T (SI Fig. S6), indicating that it is not defined by the properties of individual monolayers, but the collective property of the assembled heterostructure.

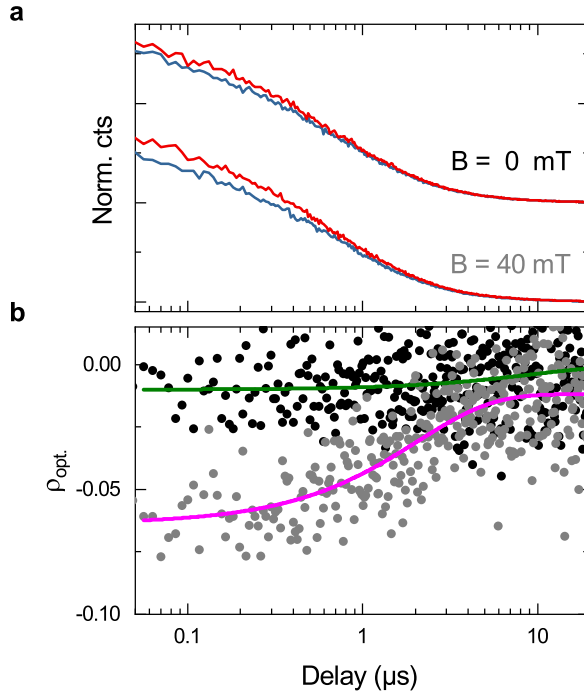


Figure 4: **Temporal evolution of iX valley polarization.** (a) Polarization-resolved iX PL decay acquired at 0 and 40 mT using σ^+ polarized excitation; blue (red) curve corresponds to PL intensity co- (cross-) polarized with the excitation laser; the data sets are offset for clarity and normalized to the intensity of co-polarized component at zero delay. (b) Time-resolved changes of ρ_{opt} for $B = 0$ mT (black) and $B = 40$ mT (gray). The solid curves are guides to the eye.

Figure 4a presents the polarization-resolved decay of iX PL recorded at 0 mT and 40 mT in a device with $B_{\text{sat}} \sim 200$ mT. The difference in intensity for cross-co polarization allows us to monitor $|\rho_{\text{opt}}|$ as a function of time. Figure 4b plots the time-resolved ρ_{opt} extracted from the iX PL decay measured at 0 mT and 40 mT; the solid curves are guides to the eye. Without magnetic field (black filled circles), iX has a low polarization degree ($|\rho_{\text{opt}}| < 2\%$) throughout the measurement range. In contrast, at $B = 40$ mT (gray filled circles) $|\rho_{\text{opt}}|$ starts at 6% and shows a gradual decay towards zero, with a characteristic $1/e$ time of

$\sim 2 \mu\text{s}$. These results indicate that the loss of valley polarization for iX is governed by at least two processes occurring at different timescales: a fast intervalley relaxation with a characteristic time shorter than 10 ns (i.e., timing resolution of our measurement) dominates at zero magnetic field. This process is suppressed at 40 mT, revealing a slower, microsecond-scale relaxation. We note that this timescale stems from both the loss of valley polarization and the decay of exciton population and therefore ultimately it provides a lower bound to the iX valley lifetime and a measure of the valley-excitonic information storage time.

In conclusion, we show that the iX in MoS₂/MoSe₂ heterobilayers is formed by electrons and holes residing at the edges of the Brillouin zone, with negligible degree of interlayer hybridization. We find that iX retains its optically induced valley polarization, with the cross-polarized iX PL stemming from the moiré-induced reversal of selection rules. Magnetic field enhances valley-polarization retention by suppressing fast intervalley scattering. The typical magnetic field required for this (≤ 200 mT) is within reach of a variety of readily accessible techniques, including assembling heterostructures on magnetic substrates,⁵⁶ or using rare-earth magnets.⁵⁷ Moreover, in some devices we observe $|\rho_{\text{opt}}|$ up to 7% at zero field, allowing for magnet-free operation. The combination of microsecond-long iX PL lifetime and the retention of valley polarization offers the prospect of combining excitonic and valleytronic functionalities in a single optoelectronic device.

Methods

Sample fabrication. All layers used for the fabrication of the electrically tunable MoS₂/MoSe₂ heterobilayer devices were produced by micromechanical cleavage of bulk crystals. Bulk TMD crystals were prepared by flux zone growth method⁵⁸ and bulk hBN crystals were grown by the temperature-gradient method.⁵⁹ Graphite crystals were sourced from NGS. The thickness of exfoliated crystals was estimated using optical contrast⁶⁰ and confirmed using photoluminescence and Raman spectroscopy for TMDs under 532-nm (2.33-eV) laser illumination (LabRAM HR Evolution, Horiba) and atomic force microscopy for hBN (Di-

mension Icon, Bruker). Electrically tunable heterobilayer devices were assembled by deterministic dry mechanical transfer using polymer stamps.^{34,35} The twist angle between the TMD layers was identified using polarization-resolved SHG⁶¹ measured at room temperature using a custom-built optical setup. The SHG laser was a Chameleon Compact Optical Parametric Oscillator providing ~ 200 fs pulses with a repetition rate of 80 MHz centered at 1320 nm. To minimize chromatic aberrations, a linearly polarized laser beam with ~ 5 -mW power was focused onto the sample using a 40x reflective objective (numerical aperture of 0.5, LMM40X-P01, Thorlabs). Polarization orientation was controlled using a super-achromatic half-wave plate (SAHWP05M-1700, Thorlabs) mounted in a motorized rotational mount. Electrical contacts to TMD layers and transparent FLG gates were created by direct laser lithography (LW-405B+, Microtech) with a positive resist (AZ5214E, MicroChemicals) followed by electron beam evaporation (PVD200Pro, Kurt J. Lesker) of 5 nm of Cr followed by 45 nm of Au. The resist excess metal layer was then lifted off by immersion in acetone and isopropanol for 30 minutes.

Photoluminescence measurements. Room-temperature PL measurements were performed using LabRAM HR Evolution Raman microscope under 532-nm (2.33-eV) laser illumination. Helicity-resolved magneto-optical measurements were performed in a close-cycle bath cryostat (Attodry 1000, Attocube) equipped with a superconducting magnet at a nominal sample temperature of 4 K. Excitation and collection light pass through a home-built confocal microscope in reflection geometry, with a 0.81 numerical aperture apochromatic objective (LT-307 APO/NIR/0.81, Attocube). The PL measurements were performed using 638-nm (1.94-eV) continuous-wave excitation (MCLS1-638, Thorlabs), with incident power below $5 \mu\text{W}$. The PL signal collected in epi-direction was isolated using a long-pass filter (FELH0700, Thorlabs) and detected by a 0.75-m spectrometer (SpectraPro 2750, Princeton Instruments) with 150 l mm^{-1} grating and a nitrogen cooled CCD camera (Spec-10, Princeton Instruments). Time-resolved measurements were performed using a single-photon avalanche photodiode (SPCM-AQRH-16-FC, Excelitas Technologies) and a time-to-digital

converter (quTAU, qutools GmbH) with 81 ps timing resolution. For these measurements, the intensity of CW laser was modulated using an acousto-optic modulator (MT350-A0.12-VIS, AA Opto Electronic), producing 200-ns pulses with the 100-kHz repetition rate. A dual-channel source meter (2612B, Keithley) was used for electric field tuning.

Acknowledgement

We acknowledge funding the EU Graphene and Quantum Flagships, ERC Grants Hetero2D, GSYNCOR, GIPR, EIC Grant CHARM, EPSRC Grants EP/K01711X/1, EP/K017144/1, EP/N010345/1, and EP/L016087/1. S.A.T acknowledges primary support from DOE-SC0020653 (materials synthesis). K.W. and T.T. acknowledge support from the JSPS KAKENHI (Grant Numbers 21H05233 and 23H02052) and World Premier International Research Center Initiative (WPI), MEXT, Japan. We thank V. Falko, C. Faugeras, and I. Paradisanos for fruitful discussions.

References

- (1) Mak, K. F.; Shan, J. Photonics and Optoelectronics of 2D Semiconductor Transition Metal Dichalcogenides. *Nat. Photonics* **2016**, *10*, 216–226.
- (2) Zhou, X.; Hu, X.; Yu, J.; Liu, S.; Shu, Z.; Zhang, Q.; Li, H.; Ma, Y.; Xu, H.; Zhai, T. 2D Layered Material-Based Van Der Waals Heterostructures for Optoelectronics. *Adv. Funct. Mater.* **2018**, *1706587*, 1706587.
- (3) Woessner, A.; Lundberg, M. B.; Gao, Y.; Principi, A.; Alonso-González, P.; Carrega, M.; Watanabe, K.; Taniguchi, T.; Vignale, G.; Polini, M.; Hone, J.; Hillenbrand, R.; Koppens, F. H. Highly Confined Low-Loss Plasmons in Graphene-Boron Nitride Heterostructures. *Nat. Mater.* **2015**, *14*, 421–425.

- (4) Ferrari, A. C. et al. Science and Technology Roadmap for Graphene, Related Two-Dimensional Crystals, and Hybrid Systems. *Nanoscale* **2015**, *7*, 4598–4810.
- (5) Montblanch, A. R.; Barbone, M.; Aharonovich, I.; Atatüre, M.; Ferrari, A. C. Layered Materials as a Platform for Quantum Technologies. *Nat. Nanotechnol.* **2023**, *18*, 555–571.
- (6) Wang, G.; Chernikov, A.; Glazov, M. M.; Heinz, T. F.; Marie, X.; Amand, T.; Urbaszek, B. Colloquium : Excitons in Atomically Thin Transition Metal Dichalcogenides. *Rev. Mod. Phys.* **2018**, *90*, 021001.
- (7) Schaibley, J. R.; Yu, H.; Clark, G.; Rivera, P.; Ross, J. S.; Seyler, K. L.; Yao, W.; Xu, X. Valleytronics in 2D Materials. *Nat. Rev. Mater.* **2016**, *1*, 16055.
- (8) Xiao, D.; Rothschild, M.; Kim, P.; Gedik, N.; Varghese, J. O.; Vitale, S. A.; Nezich, D.; Jarillo-Herrero, P. Valleytronics: Opportunities, Challenges, and Paths Forward. *Small* **2018**, *14*, 1801483.
- (9) Novoselov, K. S.; Mishchenko, A.; Carvalho, A.; Castro Neto, A. H. 2D Materials and Van Der Waals Heterostructures. *Science (80-.)*. **2016**, *353*, aac9439.
- (10) Liu, Y.; Huang, Y.; Duan, X. Van Der Waals Integration Before and Beyond Two-Dimensional Materials. *Nature* **2019**, *567*, 323–333.
- (11) Catanzaro, A. et al. Resonant Band Hybridization in Alloyed Transition Metal Dichalcogenide Heterobilayers. *Adv. Mater.* **2024**, *2309644*.
- (12) Wilson, N. P.; Yao, W.; Shan, J.; Xu, X. Excitons and Emergent Quantum Phenomena in Stacked 2D Semiconductors. *Nature* **2021**, *599*, 383–392.
- (13) Ciarrocchi, A.; Tagarelli, F.; Avsar, A.; Kis, A. Excitonic Devices With Van Der Waals Heterostructures: Valleytronics Meets Twistronics. *Nat. Rev. Mater.* **2022**, *7*, 449–464.

- (14) Mak, K. F.; Shan, J. Semiconductor Moiré Materials. *Nat. Nanotechnol.* **2022**, *17*, 686–695.
- (15) Rivera, P.; Yu, H.; Seyler, K. L.; Wilson, N. P.; Yao, W.; Xu, X. Interlayer Valley Excitons in Heterobilayers of Transition Metal Dichalcogenides. *Nat. Nanotechnol.* **2018**, *13*, 1004–1015.
- (16) Regan, E. C.; Wang, D.; Paik, E. Y.; Zeng, Y.; Zhang, L.; Zhu, J.; MacDonald, A. H.; Deng, H.; Wang, F. Emerging Exciton Physics in Transition Metal Dichalcogenide Heterobilayers. *Nat. Rev. Mater.* **2022**, *7*, 778–795.
- (17) Montblanch, A. R. et al. Confinement of Long-Lived Interlayer Excitons in WS₂/WSe₂ Heterostructures. *Commun. Phys.* **2021**, *4*, 119.
- (18) Rivera, P.; Seyler, K. L.; Yu, H.; Schaibley, J. R.; Yan, J.; Mandrus, D. G.; Yao, W.; Xu, X. Valley-Polarized Exciton Dynamics in a 2D Semiconductor Heterostructure. *Science (80-.)*. **2016**, *351*, 688–691.
- (19) Jauregui, L. A. et al. Electrical Control of Interlayer Exciton Dynamics in Atomically Thin Heterostructures. *Science (80-.)*. **2019**, *366*, 870–875.
- (20) Nayak, P. K.; Horbatenko, Y.; Ahn, S.; Kim, G.; Lee, J.-U.; Ma, K. Y.; Jang, A.-R.; Lim, H.; Kim, D.; Ryu, S.; Cheong, H.; Park, N.; Shin, H. S. Probing Evolution of Twist-Angle-Dependent Interlayer Excitons in MoSe₂/WSe₂ Van Der Waals Heterostructures. *ACS Nano* **2017**, *11*, 4041–4050.
- (21) Kunstmann, J.; Mooshammer, F.; Nagler, P.; Chaves, A.; Stein, F.; Paradiso, N.; Plechinger, G.; Strunk, C.; Schüller, C.; Seifert, G.; Reichman, D. R.; Korn, T. Momentum-Space Indirect Interlayer Excitons in Transition-Metal Dichalcogenide Van Der Waals Heterostructures. *Nat. Phys.* **2018**, *14*, 801–805.

- (22) Alexeev, E. M. et al. Resonantly Hybridized Excitons in Moiré Superlattices in Van Der Waals Heterostructures. *Nature* **2019**, *567*, 81–86.
- (23) Kremser, M.; Brotons-Gisbert, M.; Knörzer, J.; Gückelhorn, J.; Meyer, M.; Barbone, M.; Stier, A. V.; Gerardot, B. D.; Müller, K.; Finley, J. J. Discrete Interactions Between a Few Interlayer Excitons Trapped at a MoSe₂–WSe₂ Heterointerface. *npj 2D Mater. Appl.* **2020**, *4*, 8.
- (24) Ciarrocchi, A.; Unuchek, D.; Avsar, A.; Watanabe, K.; Taniguchi, T.; Kis, A. Polarization Switching and Electrical Control of Interlayer Excitons in Two-Dimensional Van Der Waals Heterostructures. *Nat. Photonics* **2019**, *13*, 131–136.
- (25) Smirnov, D. S.; Holler, J.; Kempf, M.; Zipfel, J.; Nagler, P.; Ballottin, M. V.; Mitioglu, A. A.; Chernikov, A.; Christianen, P. C. M.; Schüller, C.; Korn, T. Valley-Magnetophonon Resonance for Interlayer Excitons. *2D Mater.* **2022**, *9*, 045016.
- (26) Gerber, I. C.; Courtade, E.; Shree, S.; Robert, C.; Taniguchi, T.; Watanabe, K.; Balocchi, A.; Renucci, P.; Lagarde, D.; Marie, X.; Urbaszek, B. Interlayer Excitons in Bilayer MoS₂ With Strong Oscillator Strength up to Room Temperature. *Phys. Rev. B* **2019**, *99*, 1–8.
- (27) Barré, E.; Karni, O.; Liu, E.; O’Beirne, A. L.; Chen, X.; Ribeiro, H. B.; Yu, L.; Kim, B.; Watanabe, K.; Taniguchi, T.; Barmak, K.; Lui, C. H.; Refaely-Abramson, S.; da Jornada, F. H.; Heinz, T. F. Optical Absorption of Interlayer Excitons in Transition-Metal Dichalcogenide Heterostructures. *Science (80-.)*. **2022**, *376*, 406–410.
- (28) Seyler, K. L.; Rivera, P.; Yu, H.; Wilson, N. P.; Ray, E. L.; Mandrus, D. G.; Yan, J.; Yao, W.; Xu, X. Signatures of Moiré-Trapped Valley Excitons in MoSe₂/WSe₂ Heterobilayers. *Nature* **2019**, *567*, 66–70.
- (29) Tran, K. et al. Evidence for Moiré Excitons in Van Der Waals Heterostructures. *Nature* **2019**, *567*, 71–75.

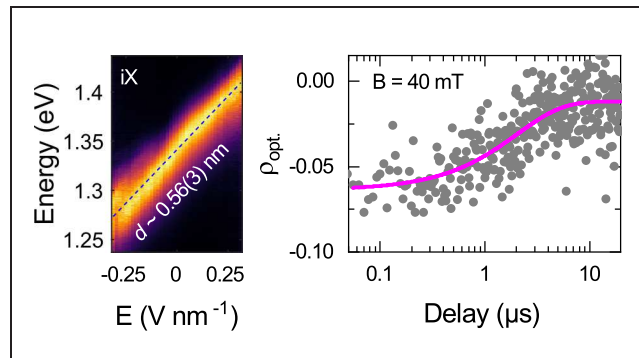
- (30) Liu, E.; Barré, E.; van Baren, J.; Wilson, M.; Taniguchi, T.; Watanabe, K.; Cui, Y.-t.; Gabor, N. M.; Heinz, T. F.; Chang, Y.-c.; Lui, C. H. Signatures of Moiré Trions in WSe₂/MoSe₂ Heterobilayers. *Nature* **2021**, *594*, 46–50.
- (31) Jin, C.; Regan, E. C.; Wang, D.; Iqbal Bakti Utama, M.; Yang, C.-S.; Cain, J.; Qin, Y.; Shen, Y.; Zheng, Z.; Watanabe, K.; Taniguchi, T.; Tongay, S.; Zettl, A.; Wang, F. Identification of Spin, Valley and Moiré Quasi-Angular Momentum of Interlayer Excitons. *Nat. Phys.* **2019**, *15*, 1140–1144.
- (32) Stansbury, C. H. et al. Visualizing Electron Localization of WS₂/WSe₂ Moiré Superlattices in Momentum Space. *Sci. Adv.* **2021**, *7*, 1–9.
- (33) Tang, Y.; Gu, J.; Liu, S.; Watanabe, K.; Taniguchi, T.; Hone, J.; Mak, K. F.; Shan, J. Tuning Layer-Hybridized Moiré Excitons by the Quantum-Confined Stark Effect. *Nat. Nanotechnol.* **2021**, *16*, 52–57.
- (34) Castellanos-Gomez, A.; Buscema, M.; Molenaar, R.; Singh, V.; Janssen, L.; van der Zant, H. S. J.; Steele, G. a. Deterministic Transfer of Two-Dimensional Materials by All-Dry Viscoelastic Stamping. *2D Mater.* **2014**, *1*, 011002.
- (35) Zomer, P. J.; Guimarães, M. H. D.; Brant, J. C.; Tombros, N.; van Wees, B. J. Fast Pick up Technique for High Quality Heterostructures of Bilayer Graphene and Hexagonal Boron Nitride. *Appl. Phys. Lett.* **2014**, *105*.
- (36) Cadore, A. R. et al. Monolayer WS₂ Electro- and Photo-Luminescence Enhancement by TFSI Treatment. *2D Mater.* **2024**, *11*, 025017.
- (37) Cadiz, F. et al. Excitonic Linewidth Approaching the Homogeneous Limit in MoS₂-Based Van Der Waals Heterostructures. *Phys. Rev. X* **2017**, *7*, 021026.
- (38) Shree, S.; Paradisanos, I.; Marie, X.; Robert, C.; Urbaszek, B. Guide to Optical Spectroscopy of Layered Semiconductors. *Nat. Rev. Phys.* **2021**, *3*, 39–54.

- (39) Lin, B.-H.; Chao, Y.-C.; Hsieh, I.; Chuu, C.-P.; Lee, C.-J.; Chu, F.-H.; Lu, L.-S.; Hsu, W.-t.; Pao, C.-w.; Shih, C.-k.; Su, J.-j.; Chang, W.-h. Remarkably Deep Moiré Potential for Intralayer Excitons in MoSe₂/MoS₂ Twisted Heterobilayers. *Nano Lett.* **2023**, *23*, 1306–1312.
- (40) Zhu, Z. Y.; Cheng, Y. C.; Schwingenschlögl, U. Giant Spin-Orbit-Induced Spin Splitting in Two-Dimensional Transition-Metal Dichalcogenide Semiconductors. *Phys. Rev. B* **2011**, *84*, 153402.
- (41) Constantinescu, G. C.; Hine, N. D. Energy Landscape and Band-Structure Tuning in Realistic MoS₂/MoSe₂ Heterostructures. *Phys. Rev. B - Condens. Matter Mater. Phys.* **2015**, *91*, 1–8.
- (42) Liu, K.; Zhang, L.; Cao, T.; Jin, C.; Qiu, D.; Zhou, Q.; Zettl, A.; Yang, P.; Louie, S. G.; Wang, F. Evolution of Interlayer Coupling in Twisted Molybdenum Disulfide Bilayers. *Nat. Commun.* **2014**, *5*, 4966.
- (43) Tebyetekerwa, M.; Zhang, J.; Saji, S. E.; Wibowo, A. A.; Rahman, S.; Truong, T. N.; Lu, Y.; Yin, Z.; Macdonald, D.; Nguyen, H. T. Twist-Driven Wide Freedom of Indirect Interlayer Exciton Emission in MoS₂/WS₂ Heterobilayers. *Cell Reports Phys. Sci.* **2021**, *2*, 100509.
- (44) He, J.; Hummer, K.; Franchini, C. Stacking Effects on the Electronic and Optical Properties of Bilayer Transition Metal Dichalcogenides MoS₂, MoSe₂, WS₂, and WSe₂. *Phys. Rev. B* **2014**, *89*, 075409.
- (45) Sung, J. et al. Broken Mirror Symmetry in Excitonic Response of Reconstructed Domains in Twisted MoSe₂/MoSe₂ Bilayers. *Nat. Nanotechnol.* **2020**, *15*, 7–12.
- (46) Nagler, P.; Ballottin, M. V.; Mitioglu, A. A.; Mooshammer, F.; Paradiso, N.; Strunk, C.; Huber, R.; Chernikov, A.; Christianen, P. C. M.; Schüller, C.; Korn, T. Giant Magnetic

- Splitting Inducing Near-Unity Valley Polarization in Van Der Waals Heterostructures. *Nat. Commun.* **2017**, *8*, 1–6.
- (47) Woźniak, T.; Faria Junior, P. E.; Seifert, G.; Chaves, A.; Kunstmann, J.; Junior, P. E. F.; Seifert, G.; Chaves, A.; Kunstmann, J. Exciton G-Factors of Van Der Waals Heterostructures From First Principles Calculations. *Phys. Rev. B* **2020**, *101*, 1–27.
- (48) Li, Y.; Ludwig, J.; Low, T.; Chernikov, A.; Cui, X.; Arefe, G.; Kim, Y. D.; Van Der Zande, A. M.; Rigosi, A.; Hill, H. M.; Kim, S. H.; Hone, J.; Li, Z.; Smirnov, D.; Heinz, T. F. Valley Splitting and Polarization by the Zeeman Effect in Monolayer MoSe₂. *Phys. Rev. Lett.* **2014**, *113*, 1–5.
- (49) Koperski, M.; Molas, M. R.; Arora, A.; Nogajewski, K.; Bartos, M.; Wyzula, J.; Vavclavkova, D.; Kossacki, P.; Potemski, M. Orbital, Spin and Valley Contributions to Zeeman Splitting of Excitonic Resonances in MoSe₂, WSe₂ and WS₂ Monolayers. *2D Mater.* **2019**, *6*.
- (50) Mak, K. F.; He, K.; Shan, J.; Heinz, T. F. Control of Valley Polarization in Monolayer MoS₂ by Optical Helicity. *Nat. Nanotechnol.* **2012**, *7*, 494–498.
- (51) Wang, G.; Palleau, E.; Amand, T.; Tongay, S.; Marie, X.; Urbaszek, B. Polarization and Time-Resolved Photoluminescence Spectroscopy of Excitons in MoSe₂ Monolayers. *Appl. Phys. Lett.* **2015**, *106*, 2–6.
- (52) MacNeill, D.; Heikes, C.; Mak, K. F.; Anderson, Z.; Kormányos, A.; Zólyomi, V.; Park, J.; Ralph, D. C. Breaking of Valley Degeneracy by Magnetic Field in Monolayer MoSe₂. *Phys. Rev. Lett.* **2015**, *114*, 037401.
- (53) Jiang, C.; Xu, W.; Rasmita, A.; Huang, Z.; Li, K.; Xiong, Q.; Gao, W. B. Microsecond Dark-Exciton Valley Polarization Memory in Two-Dimensional Heterostructures. *Nat. Commun.* **2018**, *9*, 753.

- (54) Tan, Q.; Rasmita, A.; Li, S.; Liu, S.; Huang, Z.; Xiong, Q.; Yang, S. A.; Novoselov, K. S.; Gao, W.-b. B. Layer-Engineered Interlayer Excitons. *Sci. Adv.* **2021**, *7*, 1–9.
- (55) Smoleński, T.; Kazimierczuk, T.; Goryca, M.; Molas, M. R.; Nogajewski, K.; Faugeras, C.; Potemski, M.; Kossacki, P. Magnetic Field Induced Polarization Enhancement in Monolayers of Tungsten Dichalcogenides: Effects of Temperature. *2D Mater.* **2017**, *5*, 015023.
- (56) Gibertini, M.; Koperski, M.; Morpurgo, A. F.; Novoselov, K. S. Magnetic 2D Materials and Heterostructures. *Nat. Nanotechnol.* **2019**, *14*, 408–419.
- (57) Stern, H. L.; Gu, Q.; Jarman, J.; Eizagirre Barker, S.; Mendelson, N.; Chugh, D.; Schott, S.; Tan, H. H.; Siringhaus, H.; Aharonovich, I.; Atatüre, M. Room-Temperature Optically Detected Magnetic Resonance of Single Defects in Hexagonal Boron Nitride. *Nat. Commun.* **2022**, *13*, 1–9.
- (58) Edelberg, D. et al. Approaching the Intrinsic Limit in Transition Metal Diselenides Via Point Defect Control. *Nano Lett.* **2019**, *19*, 4371–4379.
- (59) Watanabe, K.; Taniguchi, T.; Kanda, H. Direct-Bandgap Properties and Evidence for Ultraviolet Lasing of Hexagonal Boron Nitride Single Crystal. *Nat. Mater.* **2004**, *3*, 404–409.
- (60) Li, H.; Wu, J.; Huang, X.; Lu, G.; Yang, J.; Lu, X.; Xiong, Q.; Zhang, H. Rapid and Reliable Thickness Identification of Two-Dimensional Nanosheets Using Optical Microscopy. *ACS Nano* **2013**, *7*, 10344–10353.
- (61) Hsu, W. T.; Zhao, Z. A.; Li, L. J.; Chen, C. H.; Chiu, M. H.; Chang, P. S.; Chou, Y. C.; Chang, W. H. Second Harmonic Generation From Artificially Stacked Transition Metal Dichalcogenide Twisted Bilayers. *ACS Nano* **2014**, *8*, 2951–2958.

TOC Graphic



Supplementary Information for Nature of long-lived moiré interlayer excitons in electrically tunable MoS₂/MoSe₂ heterobilayers

Evgeny M. Alexeev,^{*,†,‡} Carola M. Purser,^{‡,†} Carmem M. Gilardoni,[‡] James Kerfoot,[†] Hao Chen,[†] Alisson R. Cadore,^{†,¶} Bárbara L.T. Rosa,[†] Matthew S. G. Feuer,[‡] Evans Javary,^{‡,§} Patrick Hays,^{||} Kenji Watanabe,[⊥] Takashi Taniguchi,[#] Seth Ariel Tongay,^{||} Dhiren M. Kara,[‡] Mete Atatüre,^{*,‡} and Andrea C. Ferrari^{*,†}

[†]*Cambridge Graphene Centre, University of Cambridge, 9 JJ Thomson Avenue, CB3 0FA, Cambridge, UK*

[‡]*Cavendish Laboratory, University of Cambridge, JJ Thomson Avenue, Cambridge CB3 0HE, UK*

[¶]*Brazilian Nanotechnology National Laboratory, Brazilian Center for Research in Energy and Materials, Sao Paulo, Brazil*

[§]*École Normale Supérieure, PSL, 5 Rue D'ulm Paris, 75005, France*

^{||}*Materials Science and Engineering, School for Engineering of Matter, Transport and Energy, Arizona State University, Tempe, Arizona 85287, United States*

[⊥]*Research Center for Electronic and Optical Materials, National Institute for Materials Science, 1-1 Namiki, Tsukuba 305-0044, Japan*

[#]*Research Center for Materials Nanoarchitectonics, National Institute for Materials Science, 1-1 Namiki, Tsukuba 305-0044, Japan*

E-mail: ea529@cam.ac.uk; ma424@cam.ac.uk; acf26@cam.ac.uk

Table 1: **Devices parameters.** Summary of key parameters for the devices investigated in this study: twist angle (θ), fast and slow time constant for iX PL decay (τ_1 and τ_2), effective iX g-factor (g), optically-induced valley polarization in the absence of magnetic field and at saturation (ρ_{PL}^0 and $\rho_{\text{PL}}^{\text{sat.}}$), and saturation magnetic field for ρ_{PL} ($B_{\text{sat.}}$).

Device #	$\theta, ^\circ$	$\tau_1, \mu\text{s}$	$\tau_2, \mu\text{s}$	g	ρ_{PL}^0	$\rho_{\text{PL}}^{\text{sat.}}$	$B_{\text{sat.}}, T$
1	4	0.03	0.13	+6.0	-0.07	-0.13	3
2	1	1.0	4.4	+6.7	-0.04	-0.11	1.25
3	3	0.14	0.56	+2.5	-0.01	-0.07	0.02
4	1	0.33	2.2	+2.7	-0.03	-0.10	≤ 0.25
5	3	0.3	1.7	+1.0	-0.01	-0.09	≤ 1
6	1	0.8	3.0	+8.0	0.0	-0.06	0.2

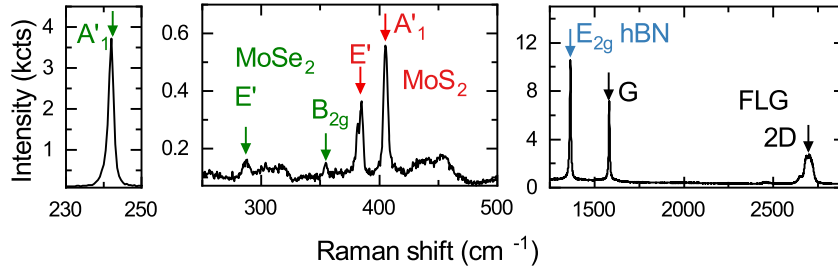


Figure S1: **Raman spectroscopy.** Raman spectra from the device, acquired at room temperature using 2.33 eV optical excitation. Dominant peaks in the 50-500 cm^{-1} range correspond to in-plane A'_1 mode at 241.9 (405.4) cm^{-1} and out-of-plane E' mode at 286.7 (384.0) cm^{-1} of MoSe₂ (MoS₂).¹ The peak at 354.7 cm^{-1} is out-of-plane B_{2g} mode of MoSe₂, which is Raman inactive on monolayers,² but becomes active in few-layers and heterobilayers due to the reduction of symmetry elements.³ Higher-frequency range shows E_{2g} mode at from hBN encapsulation layers at 1365 cm^{-1} ⁴ and the G and $2D$ Raman modes from FLG gates, at 1582 and ~ 2697 cm^{-1} ,⁵ respectively.

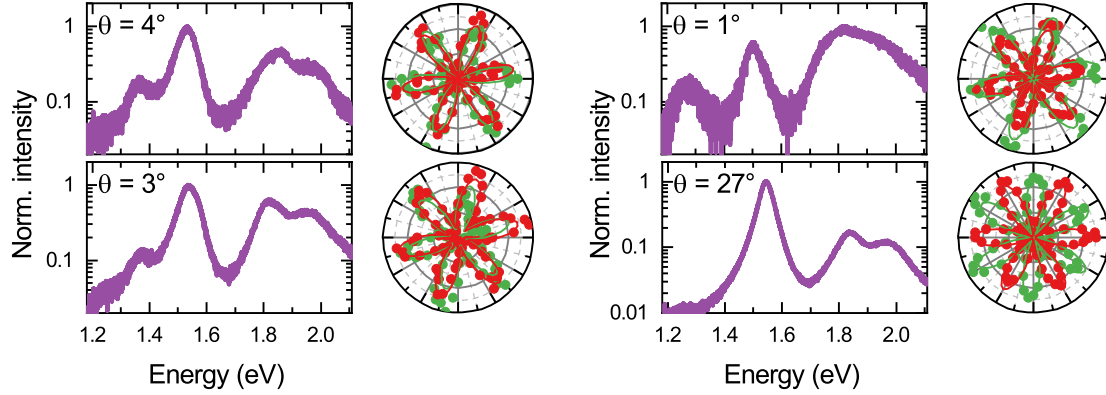


Figure S2: **Twist angle effects.** Normalized PL spectra and polar plots of polarization-resolved SHG signals acquired at room temperature in four devices with different rotational alignment between the TMD layers. Three devices with close rotational alignment ($\theta \leq 5^\circ$) show iX peak in the PL spectrum, which is not present in the PL spectrum of the strongly misaligned device ($\theta \approx 27^\circ$).

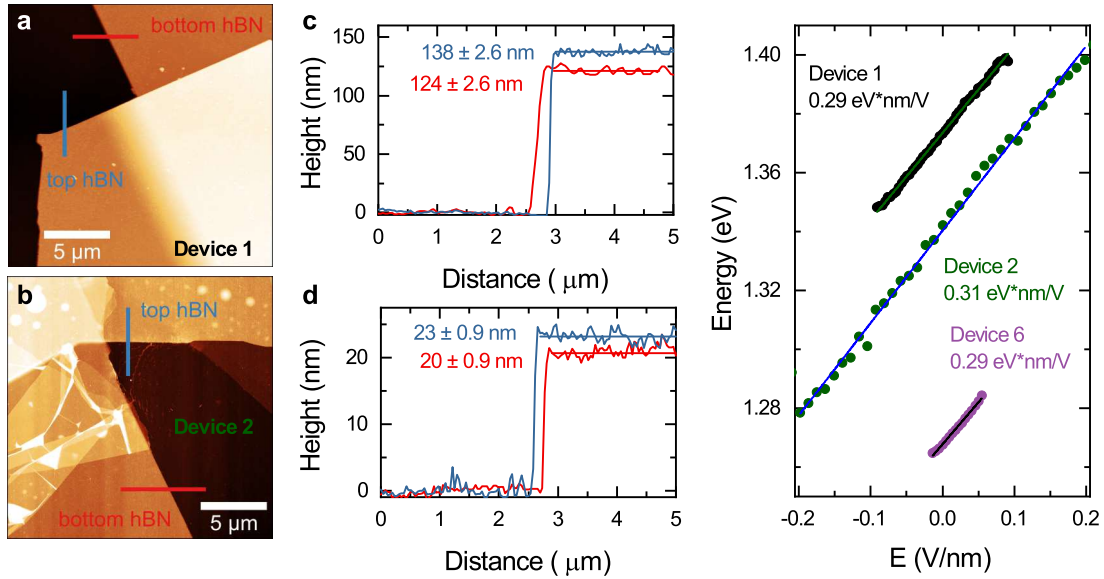


Figure S3: **Dipole size identification.** (a-c) (a and b) AFM topography images of devices 1 and 2 acquired at the edges of top and bottom hBN encapsulation layers and (c and d) cross-sections taken at the positions identified by the corresponding colour lines, showing the thickness of the layers. (e) Change of iX emission energy under applied out-of-plane electric field measured in Devices 1, 2, and 6. The rate of change of ~ 0.3 eV V/nm extracted from the linear fit corresponds to the dipole size of ~ 0.55 nm.

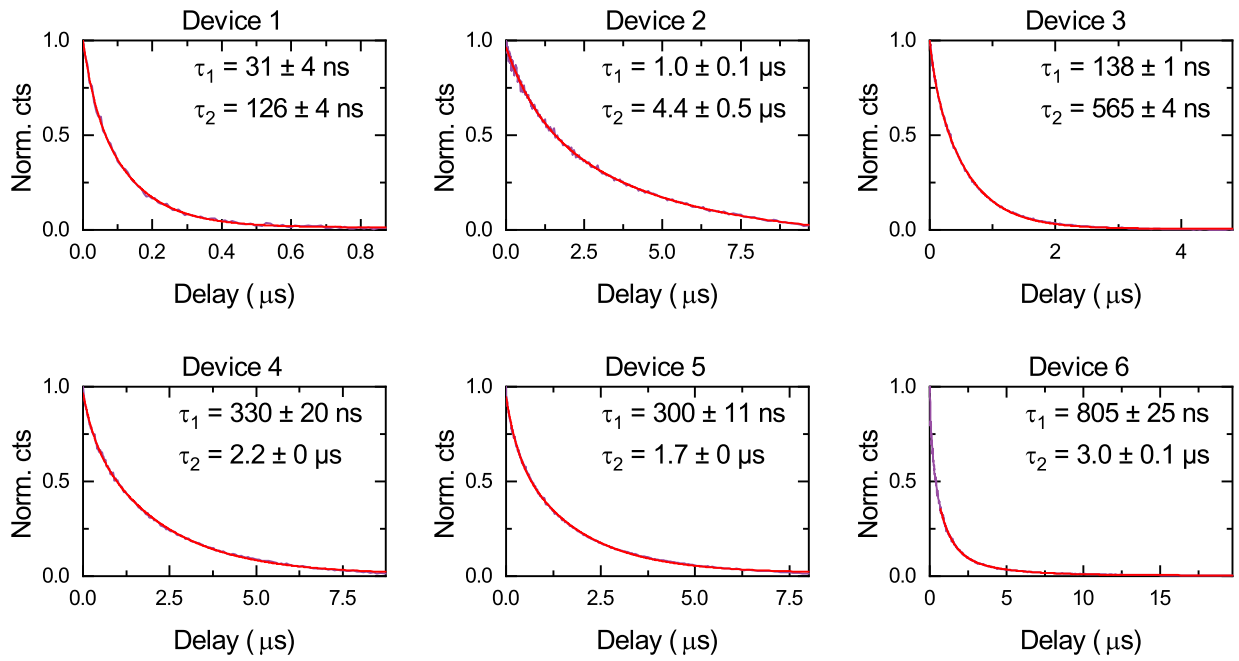


Figure S4: **iX lifetimes.** iX PL decay acquired in Devices 1-6. Solid red lines are bi-exponential fits to the data, time constants extracted from the fit are presented next to each curve.

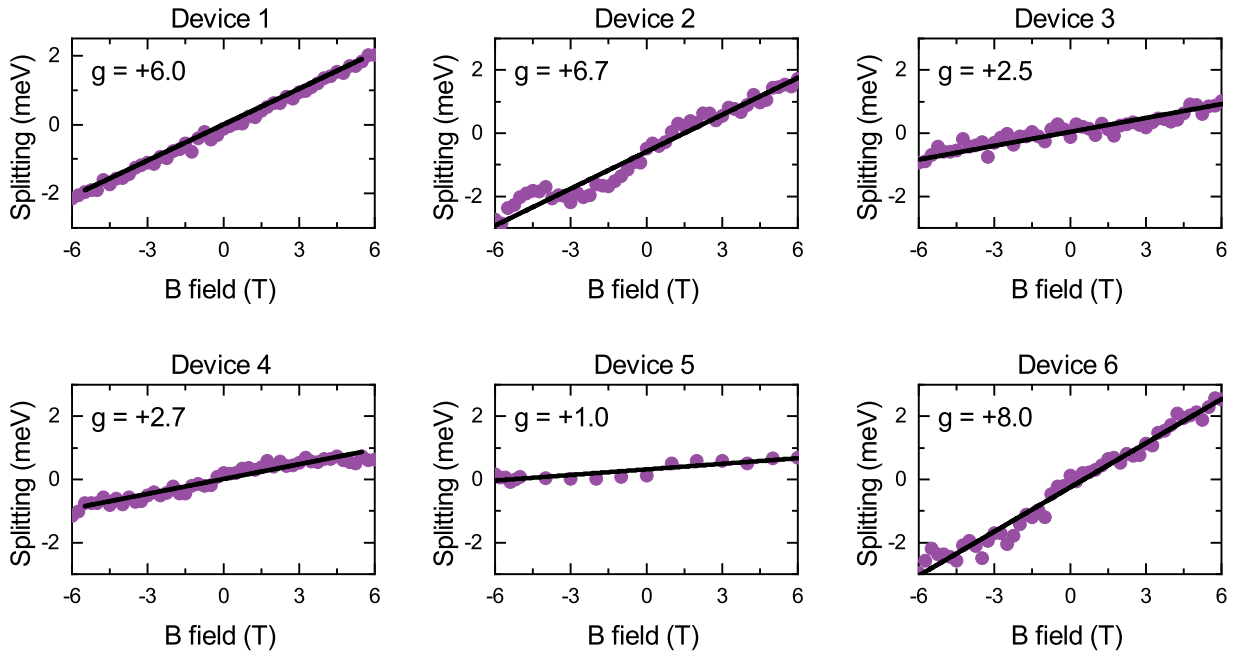


Figure S5: **iX effective g-factors.** Energy splitting between σ^+ and σ^- polarized PL as a function of out-of-plane magnetic field for Devices 1-6. Landé g factors extracted using linear fitting are listed next to each plot.

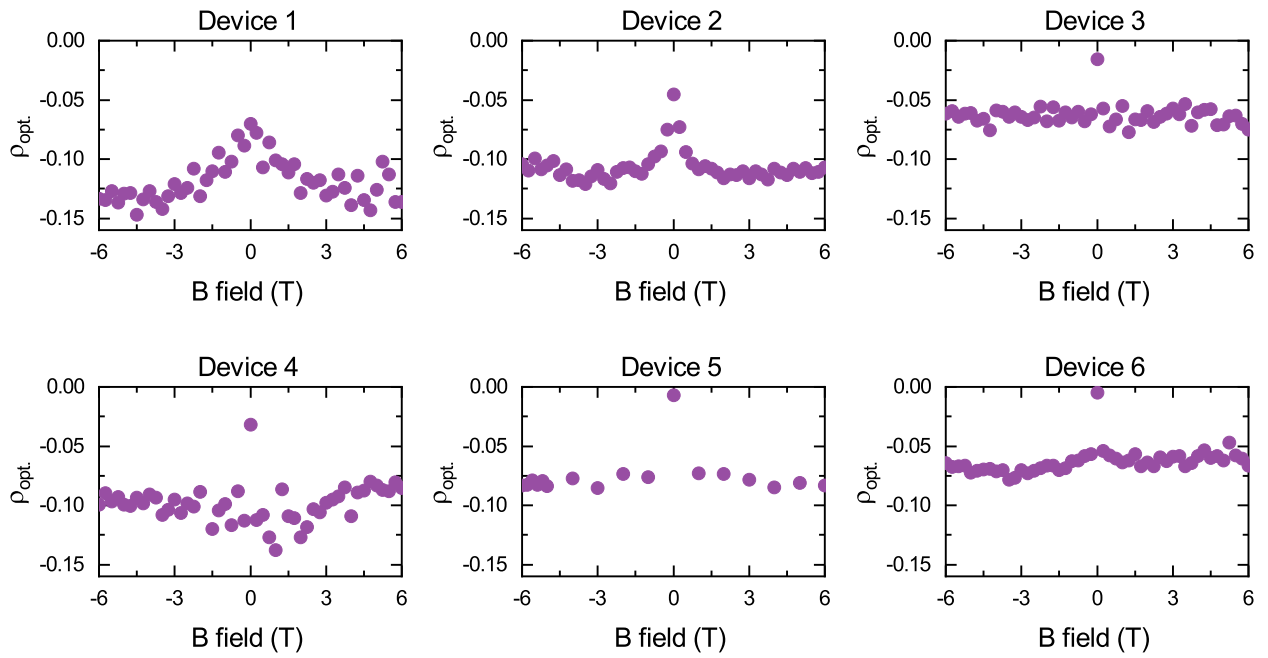


Figure S6: **Optically induced valley polarization.** Changes of optically induced iX PL valley polarization under applied magnetic field for Devices 1-6.

References

- (1) Terrones, H.; Del Corro, E.; Feng, S.; Poumirol, J. M.; Rhodes, D.; Smirnov, D.; Pradhan, N. R.; Lin, Z.; Nguyen, M. A.; Elías, A. L.; Mallouk, T. E.; Balicas, L.; Pimenta, M. A.; Terrones, M. New First Order Raman-Active Modes in Few Layered Transition Metal Dichalcogenides. *Sci. Rep.* **2014**, *4*, 1–9.
- (2) Tonndorf, P.; Schmidt, R.; Böttger, P.; Zhang, X.; Börner, J.; Liebig, A.; Albrecht, M.; Kloc, C.; Gordan, O.; Zahn, D. R. T.; Michaelis de Vasconcellos, S.; Bratschitsch, R. Photoluminescence Emission and Raman Response of Monolayer MoS₂, MoSe₂, and WSe₂. *Opt. Express* **2013**, *21*, 4908.
- (3) Pan, Y.; Li, S.; Rahaman, M.; Milekhin, I.; Zahn, D. R. T. Signature of Lattice Dynamics in Twisted 2D Homo/hetero-Bilayers. *2D Mater.* **2022**, *9*, 045018.
- (4) Reich, S.; Ferrari, A. C.; Arenal, R.; Loiseau, A.; Bello, I.; Robertson, J. Resonant Raman Scattering in Cubic and Hexagonal Boron Nitride. *Phys. Rev. B - Condens. Matter Mater. Phys.* **2005**, *71*, 1–12.
- (5) Ferrari, A. C.; Meyer, J. C.; Scardaci, V.; Casiraghi, C.; Lazzeri, M.; Mauri, F.; Piscanec, S.; Jiang, D.; Novoselov, K. S.; Roth, S.; Geim, A. K. Raman Spectrum of Graphene and Graphene Layers. *Phys. Rev. Lett.* **2006**, *97*, 1–4.